

HPSTAR  
0133—2015

# Synthesis, Structure, and Pressure-Induced Polymerization of $\text{Li}_3\text{Fe}(\text{CN})_6$ Accompanied with Enhanced Conductivity

Kuo Li,\*<sup>†,‡</sup> Haiyan Zheng,\*<sup>†,‡</sup> Takanori Hattori,<sup>§</sup> Asami Sano-Furukawa,<sup>§</sup> Christopher A. Tulk,<sup>||</sup> Jamie Molaison,<sup>||</sup> Mikhail Feygenson,<sup>||</sup> Ilia N. Ivanov,<sup>⊥</sup> Wenge Yang,<sup>†,△</sup> and Ho-kwang Mao<sup>†,‡</sup>

<sup>†</sup>Center for High Pressure Science and Technology Advanced Research, Beijing, 100094, China

<sup>‡</sup>Geophysical Laboratory, Carnegie Institution of Washington, Washington, District of Columbia 20015, United States

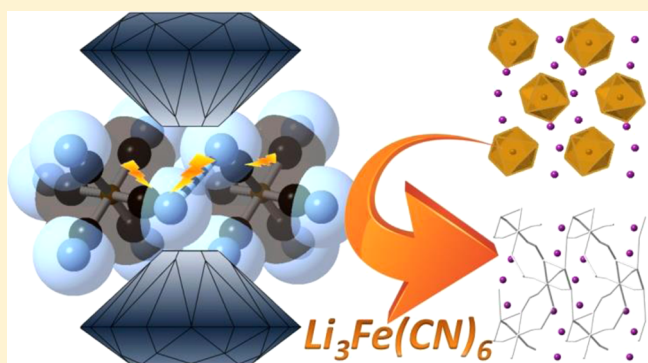
<sup>§</sup>Japan Proton Accelerator Research Complex Center, Japan Atomic Energy Agency, Tokai, Ibaraki 319-1195, Japan

<sup>||</sup>Spallation Neutron Source and <sup>⊥</sup>Center for Nanophase Materials Sciences, Oak Ridge National Laboratory, Oak Ridge, Tennessee 37830, United States

<sup>△</sup>HPSynC, Geophysical Laboratory, Carnegie Institution of Washington, Argonne, Illinois 60439, United States

## Supporting Information

**ABSTRACT:** Pressure-induced polymerization of charged triple-bond monomers like acetylide and cyanide could lead to formation of a conductive metal–carbon network composite, thus providing a new route to synthesize inorganic/organic conductors with tunable composition and properties. The industry application of this promising synthetic method is mainly limited by the reaction pressure needed, which is often too high to be reached for gram amounts of sample. Here we successfully synthesized highly conductive  $\text{Li}_3\text{Fe}(\text{CN})_6$  at maximum pressure around 5 GPa and used *in situ* diagnostic tools to follow the structural and functional transformations of the sample, including *in situ* X-ray and neutron diffraction and Raman and impedance spectroscopy, along with the neutron pair distribution function measurement on the recovered sample. The cyanide anions start to react around 1 GPa and bond to each other irreversibly at around 5 GPa, which are the lowest reaction pressures in all known metal cyanides and within the technologically achievable pressure range for industrial production. The conductivity of the polymer is above  $10^{-3}$  S·cm<sup>-1</sup>, which reaches the range of conductive polymers. This investigation suggests that the pressure-induced polymerization route is practicable for synthesizing some types of functional conductive materials for industrial use, and further research like doping and heating can hence be motivated to synthesize novel materials under lower pressure and with better performances.



## INTRODUCTION

Pressure-induced polymerization (PIP) of alkynes and nitriles at high pressure (usually several to tens of gigapascals) produces polymerized conjugated double bonds, which are usually electrically conductive (after doping).<sup>1</sup> The PIP approach can be applied to a wide variety of materials, including charged unsaturated ions like  $\text{C}_2^{2-}$  and  $\text{CN}^-$ , which can overcome electrostatic repulsion barriers and polymerize.<sup>1b,2</sup> The approach provides an interesting route to build a metal–carbon network composite, with functional components like metallic cations embedded into the structure of conductive materials. The materials are expected to be electrochemically active and ionically conductive, which can potentially be used as cathode materials for batteries, just like Prussian blue.<sup>3</sup> However, the required pressure for polymerization of most metal cyanides and acetylates is usually tens of gigapascals,<sup>1b,2,4</sup> which is too high for industrial processes. Thus, it is important

to find low-pressure reaction routes leading to the formation of these promising materials.

In the PIP of  $\text{K}_3\text{Fe}(\text{CN})_6$ ,  $\text{Fe}^{3+}$  accepts an electron from  $\text{CN}^-$ , reducing the charge density of  $\text{CN}^-$  and promoting bonding between them.<sup>5</sup> The reaction pressure is significantly lower than that of alkali metal cyanide, and the electronic conductivity is enhanced by 3 orders of magnitude, making it suitable for application as the cathode material of an alkaline metal battery. However, the reaction pressure of the irreversible bonding between  $\text{CN}^-$  is around 8 GPa at room temperature, which is still too high for industrial application. To further decrease the reaction pressure, the starting materials need to be properly tailored. Smaller interspaced cations like  $\text{Li}^+$  are expected to lower the reaction pressure. Here we synthesized anhydrous  $\text{Li}_3\text{Fe}(\text{CN})_6$ , determined its crystal structure by

Received: August 12, 2015

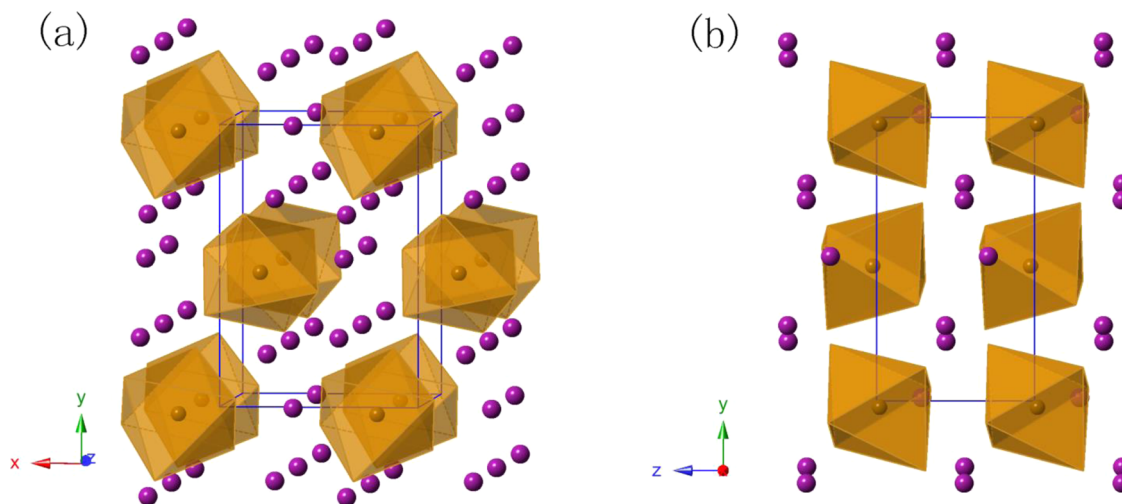


**Figure 1.** Crystal structure of  $\text{Li}_3\text{Fe}(\text{CN})_6$ , viewed along (a) approximately [001] and (b) [100]. The brown octahedron stands for  $\text{Fe}(\text{CN})_6^{3-}$  and the purple atom stands for  $\text{Li}^+$ ; C and N are omitted for clarity.

neutron diffraction, and investigated its PIP process by X-ray and neutron diffraction, neutron pair distribution function (PDF), and Raman and impedance spectroscopy. By using the smaller  $\text{Li}^+$ , we successfully reduced the reaction pressure, forcing the cyanide ions to react at around 1 GPa and polymerize irreversibly at around 4–5 GPa, which can be realized on the industrial scale. At higher pressure, the PIP reaction continues, leading to further increases in conductivity. Our investigation suggests that the PIP of  $\text{Li}_3\text{Fe}(\text{CN})_6$  is a practical and potentially scalable synthetic approach to prepare carbon-based functional conductors.

## ■ EXPERIMENTAL SECTION

**Synthesis and Structure Determination.** Stoichiometric amounts of  $\text{K}_3\text{Fe}(\text{CN})_6$  and  $\text{AgNO}_3$  were dissolved in deionized water separately, and the solutions were then mixed by stirring.  $\text{Ag}_3\text{Fe}(\text{CN})_6$  was precipitated and washed with deionized water to remove residual  $\text{K}^+$  and  $\text{NO}_3^-$ . The product was dried in air and dispersed in a cold ( $\sim 0^\circ\text{C}$ )  $\text{LiCl}$  solution cooling in an ice bath. An additional 10%  $\text{Ag}_3\text{Fe}(\text{CN})_6$  is added to precipitate all the chloride anions. The white precipitate ( $\text{AgCl}$ ) and the residual  $\text{Ag}_3\text{Fe}(\text{CN})_6$  were filtered, and the solution was dried in a freeze-dryer. The yellow product [ $\text{Li}_3\text{Fe}(\text{CN})_6 \cdot 2\text{H}_2\text{O}$ ] was then heated up to 140–150 °C for 20–30 min in a glovebox with water and oxygen content around 1 ppm, to obtain the anhydrous  $\text{Li}_3\text{Fe}(\text{CN})_6$  sample.  ${}^7\text{Li}$  isotope and deuterated water were used in the synthesis of sample for neutron experiments. X-ray diffraction patterns of  $\text{Li}_3\text{Fe}(\text{CN})_6$  and its hydrate were collected on a lab X-ray diffractometer (XRD) with a Bragg–Brentano geometry. Samples were sealed by Kapton tape to keep moisture out. Neutron diffraction patterns at ambient pressure were collected in a sealed vanadium can at beamline 3 (SNAP), Spallation Neutron Source (SNS), Oak Ridge National Lab (ORNL), and beamline 11 (PLANET).<sup>6</sup> Material and Life Science Experimental Facility, Japan Proton Accelerator Research Complex (J-PARC).

**High-Pressure Experiments.** In situ high-pressure neutron diffraction data were collected on the 6-axis press<sup>7</sup> at PLANET, J-PARC.  $\text{Li}_3\text{Fe}(\text{CN})_6$  powder was loaded to an aluminum chamber as a 1:1 mixture by volume of Fluorinert FC-70 and FC-77 as the pressure medium. The pressure on the sample was precalibrated. For in situ Raman and XRD measurements, a fine powder of  $\text{Li}_3\text{Fe}(\text{CN})_6$  was gently ground in an agate mortar for less than 5 min before being loaded into a symmetric-style diamond anvil cell (DAC)<sup>8</sup> fitted with diamonds polished to culets with diameter  $d_{\text{culet}} = 400\text{ }\mu\text{m}$ . T301 stainless steel gaskets were preindented to thickness of  $\sim 30\text{ }\mu\text{m}$ , and holes with diameter  $d = 200\text{ }\mu\text{m}$  were drilled at the center of the

indentation to serve as the sample chamber. Ruby fluorescence was used for pressure calibration in the experiments.<sup>9</sup> The Raman data were collected on a laboratory-made spectrometer equipped with a second-harmonic Nd:YAG laser (operating at 532 nm) in a backscattering geometry for excitation and signal collection. In situ high-pressure XRD data were collected at 16-ID-B at Advanced Photon Source (APS), Argonne National Laboratory, with wavelength  $\lambda = 0.40663\text{ \AA}$ . Neon was loaded as pressure medium via GSECARS' gas loading system at sector 13 of APS.<sup>10</sup> The XRD data were reduced by use of the program Fit2D<sup>11</sup>.

In situ impedance spectroscopy was performed on an alternating current (ac) impedance spectroscopy system based on Zahner analyzer IM6 at the Center for Nanophase Materials Sciences, ORNL. A symmetric DAC fitted with diamonds with  $d_{\text{culet}} = 500\text{ }\mu\text{m}$  was used in a four-probe (van der Pauw<sup>12</sup>) setting, and ac voltage (50 mV) was applied in the frequency range between 0.1 Hz and 1 MHz. A steel-supported boron nitride (BN) gasket and Pt foil electrodes were used for this measurement. The gasket was preindented to  $\sim 40\text{ }\mu\text{m}$  thickness, and a hole with diameter  $\sim 200\text{ }\mu\text{m}$  was drilled at the indentation center. No pressure medium was used in the impedance measurements to keep a good connection between sample and electrodes. Ruby fluorescence was used for pressure calibration in the experiments.<sup>9</sup>

The recovered polymerized  $\text{Li}_3\text{Fe}(\text{CN})_6$  was obtained by using the VX3 Paris–Edinburgh (PE) cell with sintered diamond anvils at SNAP.<sup>13</sup> The pressure is precalibrated. The samples recovered from 2.5, 5, 7.5, 10, 12.5, 15, 17.5, and 20 GPa are loaded in 2 mm quartz capillaries for neutron total scattering experiment at Nanoscale Ordered Materials Diffractometer (NOMAD), SNS.<sup>14</sup> Data presented were reduced by the autoreduction program of NOMAD with  $Q_{\text{max}} = 31.4\text{ \AA}^{-1}$  and convoluted by Lorch function.

## ■ RESULTS AND DISCUSSION

**Synthesis and Determination of Crystal Structure.** Although  $\text{Li}_3\text{Fe}(\text{CN})_6$  was used as an organic electrolyte for many years,<sup>15</sup> research on its anhydrous solid is scarcely seen.  $\text{Li}_3\text{Fe}(\text{CN})_6$  absorbs water from humid air quickly to form  $\text{Li}_3\text{Fe}(\text{CN})_6 \cdot 2\text{H}_2\text{O}$ , which absorbs water further to form solutions. If heated up in the air,  $\text{Li}_3\text{Fe}(\text{CN})_6 \cdot 2\text{H}_2\text{O}$  transforms to an unknown powder of mixed phases,<sup>16</sup> hence inert atmosphere is needed during the dehydration. Crystal structures of  $\text{Li}_3\text{Fe}(\text{CN})_6$  were determined ab initio by X-ray and neutron diffraction. The structural model of  $\text{Li}_3\text{Fe}(\text{CN})_6$  is shown in Figure 1, the atomic coordinates are shown in Table S1, and the Rietveld plot is shown in Figure 2. At ambient

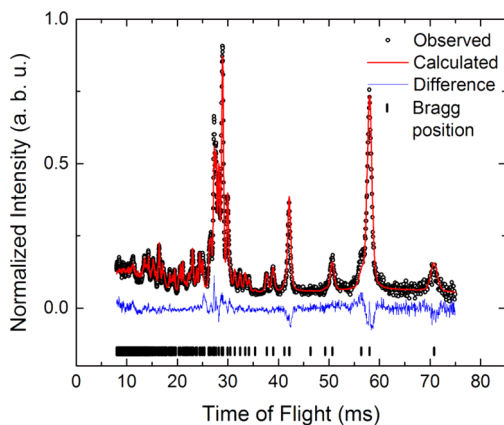


**Figure 2.** Plot of Rietveld refinement of  $\text{Li}_3\text{Fe}(\text{CN})_6$  at ambient conditions. Black circles, red line, blue line, and black bars are for observed data, calculated data, difference, and Bragg positions, respectively.

pressure and room temperature,  $\text{Li}_3\text{Fe}(\text{CN})_6$  crystallizes in a monoclinic unit cell with space group  $P2_1$  and lattice parameters  $a = 7.50 \text{ \AA}$ ,  $b = 10.69 \text{ \AA}$ ,  $c = 5.98 \text{ \AA}$ , and  $\beta = 95.5^\circ$  (referred to as phase I hereafter). In comparison with the costacking of  $\text{K}^+$  and  $\text{Fe}(\text{CN})_6^{3-}$  in  $\text{K}_3\text{Fe}(\text{CN})_6$ ,  $\text{Fe}(\text{CN})_6^{3-}$  in  $\text{Li}_3\text{Fe}(\text{CN})_6$  forms close-packed layers arranged approximately perpendicularly to one another.  $\text{Li}^+$  is located mainly between the  $\text{Fe}(\text{CN})_6^{3-}$  layers and is too small to separate  $\text{Fe}(\text{CN})_6^{3-}$  completely. The nearest N···N distance between neighbored  $\text{Fe}(\text{CN})_6^{3-}$  in  $\text{Li}_3\text{Fe}(\text{CN})_6$  is around  $3.2 \text{ \AA}$ , approximately the sum of averaged van der Waals radii of nitrogen atom ( $3.1 \text{ \AA}$ ),<sup>17</sup> while that in  $\text{K}_3\text{Fe}(\text{CN})_6$  is around  $3.8 \text{ \AA}$ .<sup>18</sup> This indicates that in  $\text{Li}_3\text{Fe}(\text{CN})_6$  the N atoms of neighbored  $\text{Fe}(\text{CN})_6^{3-}$  are touching each other directly. In contrast, in  $\text{K}_3\text{Fe}(\text{CN})_6$ ,  $\text{K}^+$  separates the  $\text{Fe}(\text{CN})_6^{3-}$  groups and is actually a barrier in the reaction between  $\text{Fe}(\text{CN})_6^{3-}$ . The distance between  $\text{Fe}(\text{CN})_6^{3-}$  groups needs to be compressed to allow the neighbored  $\text{Fe}(\text{CN})_6^{3-}$  to contact with each other before the reaction takes place. This short distance between  $\text{Fe}(\text{CN})_6^{3-}$  groups in  $\text{Li}_3\text{Fe}(\text{CN})_6$  will facilitate the intergroup addition reactions significantly, as shown later.

**Structural Transition under High Pressure. Neutron Diffraction.** The crystal structure of  $\text{Li}_3\text{Fe}(\text{CN})_6$  under external

pressure was studied by *in situ* neutron diffraction. The structure model is shown in Figure 3, the Rietveld refinement plot is shown in Figure 4, the results of the refinement are

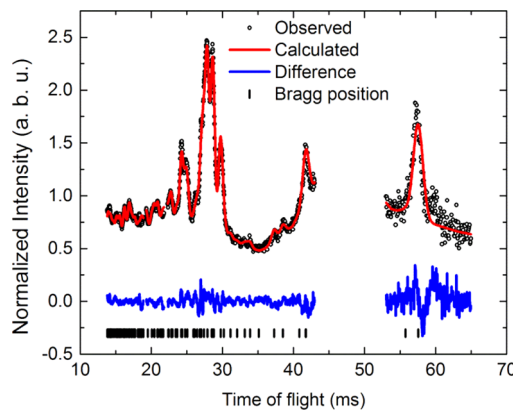


**Figure 4.** Plot of Rietveld refinement of  $\text{Li}_3\text{Fe}(\text{CN})_6$  at  $0.8 \text{ GPa}$ . Black circles, red line, blue line, and black bars are for observed data, calculated data, difference, and Bragg position, respectively. The broad hump from Fluorinert and peaks from Al chamber are masked.

shown in Table 1, and the atomic coordinates are shown in Table S2. At  $0.8 \text{ GPa}$ , the  $\text{Fe}(\text{CN})_6^{3-}$  complex anion is severely distorted, while its stacking remains nearly unchanged. This is quite different from most of the pressure-induced phase transitions of the molecular crystals, in which the packings are easily changed and the molecular structures are relatively rigid. This also suggests that the Fe–C–N and the C–Fe–C connections are the easiest to be distorted against the electrostatic repulsion between  $\text{Fe}(\text{CN})_6^{3-}$ . The distortion may promote reaction between the neighbored cyanide ions coordinating to the same  $\text{Fe}^{3+}$ , as reported in our previous  $\text{K}_3\text{Fe}(\text{CN})_6$  paper,<sup>5</sup> and evidenced by Raman experiments mentioned later. At higher pressure, Fluorinert cannot provide good hydrostaticity and thus the data cannot be used for Rietveld refinement. As shown later,  $\text{Li}_3\text{Fe}(\text{CN})_6$  transforms to another polymorph (referred to as phase II hereafter) at a certain pressure between  $0.8$  and  $2 \text{ GPa}$ .

**X-ray Diffraction.** To study the phase transitions above  $1 \text{ GPa}$ , an *in situ* synchrotron XRD experiment was performed

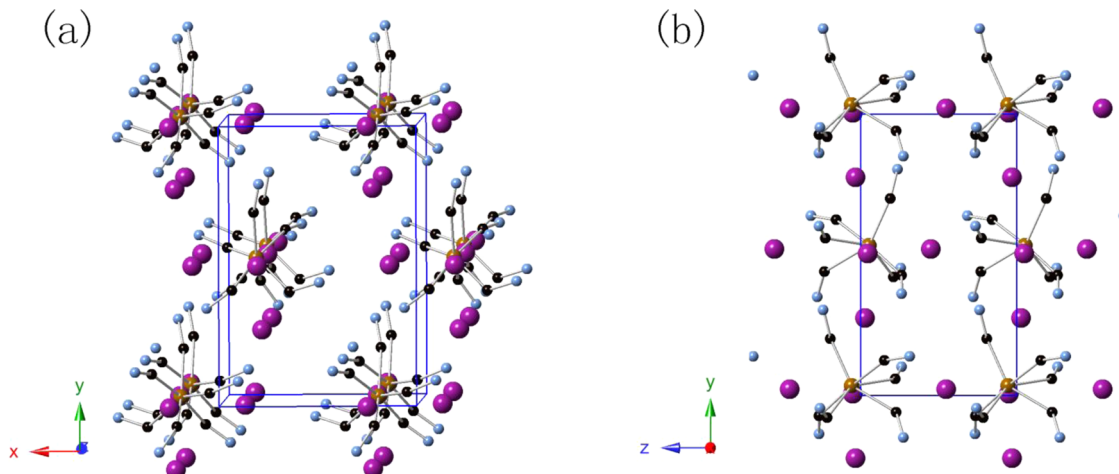


**Figure 3.** Crystal structure of  $\text{Li}_3\text{Fe}(\text{CN})_6$  at  $0.8 \text{ GPa}$ , viewed along (a) approximately  $[001]$  and (b)  $[100]$ . Brown, black, blue, and purple atoms represent Fe, C, N, and Li, respectively.

**Table 1. Collection Conditions for Neutron Diffraction and Crystallographic Data and Results of Rietveld Analysis for  $\text{Li}_3\text{Fe}(\text{CN})_6$  at 298 K**

	0 GPa	0.8 GPa
Crystal Data		
chemical formula	${}^7\text{Li}_3\text{Fe}(\text{CN})_6$	
$M_n$ , g·mol <sup>-1</sup>	233.00	
space group (number)	$P2_1$ (4)	
lattice parameters		
$a$ , Å	7.4993(8)	7.446(2)
$b$ , Å	10.6847(11)	10.580(3)
$c$ , Å	5.9764(7)	5.9091(14)
$\beta$ , deg	95.495(10)	95.64(3)
$V$ , Å <sup>3</sup>	476.68(9)	463.3(2)
$Z$	2	
$D_w$ , Mg·m <sup>-3</sup>	1.62	1.67
radiation type	neutron (unpolarized), time-of-flight	
Data Collection		
diffractometer	BL-11 (PLANET), MLF, J-PARC	
data collection method	Debye–Scherrer geometry	
specimen mounting	vanadium container	aluminum chamber in 6-axis press
detector	PSD	
data collection mode	transmission	
Refinement		
$R_p$	0.0821	0.0419
$R_{wp}$	0.0868	0.0375
$\chi^2$	2.66	2.25
$R_{\text{expected}}$	0.0326	0.0166
no. of data points	2238	1298
no. of parameters	54	57
no. of restraints	18	12
computer program	JANA2006 <sup>19</sup>	

with neon as pressure medium, which serves as a much better hydrostatic environment. The XRD pattern collected above 1.63 GPa is completely different from that at ambient pressure (Figure S1 in Supporting Information), which evidences the phase transition around 1 GPa. Benefiting from the good hydrostaticity provided by neon, another two transitions

starting at 4–5 GPa and 10–11 GPa (referred as II–III and III–IV hereafter) can be identified from the XRD patterns (Figure 5). Above 5 GPa, the peak at  $3.6^\circ$  splits, and the intensity of the peak at  $3.52^\circ$  (6.27 GPa) keeps increasing while that of the peaks at around  $3.67^\circ$  (6.27 GPa) keeps decreasing. This also suggests that between 5 and 10 GPa the sample may contain mixed II–III phases, and the transition from phase II to phase III is still ongoing with increasing external pressure. Above 10 GPa, the peak at  $3.6^\circ$  (10.29 GPa) shifts to  $3.7^\circ$  (12.52 GPa) abruptly and moves to high  $d$ -spacing slightly with increasing pressure, which indicates another phase transition (III–IV). A common feature of the phase transitions at 5 and 10 GPa is that the XRD patterns do not change dramatically, which suggests the crystal structure was not reconstructed, and the transitions are most likely induced by some local reactions, as evidenced by the Raman measurement, which will be discussed later.

**Reaction between Cyanide. In Situ Raman Spectroscopy.** The phase transitions most likely result from the reaction between cyanide anions, which can be identified by Raman spectroscopy. Raman spectra of the CN stretching mode,  $\nu(\text{CN})$ , are shown in Figure S2. The intensity of  $\nu(\text{CN})$  decreases above 1 GPa and remains unchanged up to 5 GPa, above which the  $\nu(\text{CN})$  peak disappears in the background. These two phase transitions are consistent with the transitions uncovered by diffraction experiments. The weakening of the  $\nu(\text{CN})$  peak above 1 GPa may be attributed to the reaction between parts of CN groups during the phase transition I–II. All of the  $\text{CN}^-$  anions are reacted above 5 GPa during the II–III phase transition, which is similar to the reaction in  $\text{K}_3\text{Fe}(\text{CN})_6$  at 8 GPa<sup>1d</sup> but at a significantly lower pressure that can be reached by an industrial apparatus.

**Neutron Pair Distribution Function.** Strong evidence supporting the reaction between  $\text{CN}^-$  comes from neutron PDF analysis.  $G(r)$  patterns of  $\text{Li}_3\text{Fe}(\text{CN})_6$  recovered from high pressure are shown in Figure 6. The peak at 1.1 Å corresponds to the C–N triple bond (Figure 6a). Its intensity decreases above 5 GPa with increasing pressure up to above 10 GPa. A shoulder in the range 1.3–1.5 Å rises simultaneously, which corresponds to the formation of conjugated C=N bonds. Conjugated C=N bonds are also evidenced by the peak rising at around 2.4 Å (Figure 6b). This is the distance between the atom and its next nearest neighbors in the  $\text{sp}^2$ -conjugated chain

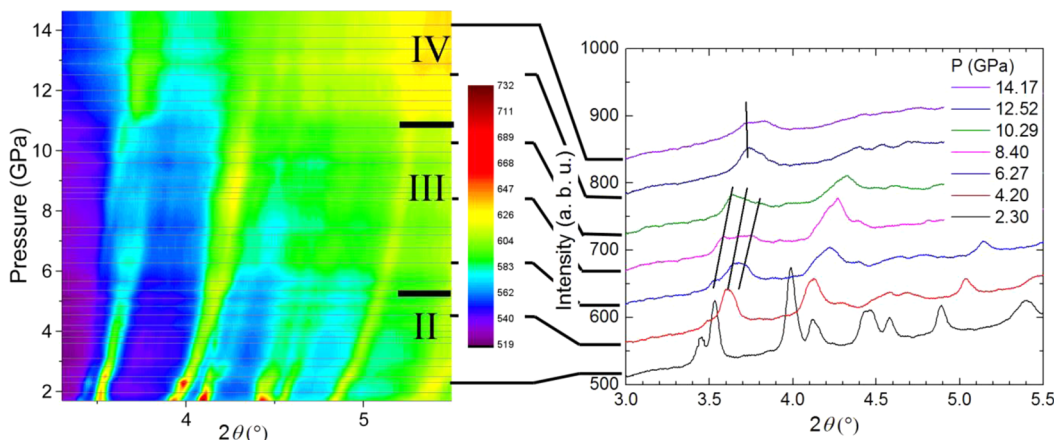


**Figure 5.** Powder XRD patterns of  $\text{Li}_3\text{Fe}(\text{CN})_6$  under external pressure in two dimensions. Intensities are represented by different colors, and selected patterns are shown in one dimension on the right. The solid lines are guides for the eyes. More 1D XRD patterns are shown in Figure S1 in Supporting Information.

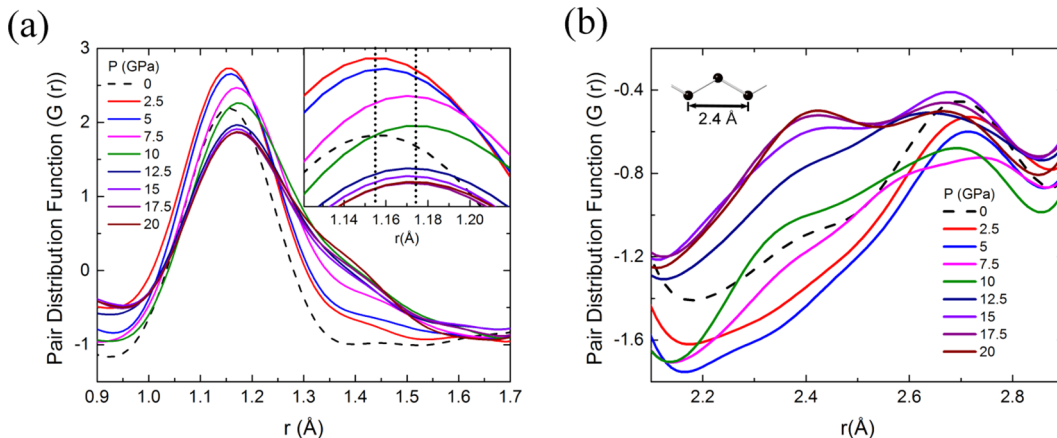


**Figure 6.** Neutron PDF patterns [ $G(r)$ ] of  $\text{Li}_3\text{Fe}(\text{CN})_6$  recovered from high pressure. PDF plots with (a)  $r = 0.9\text{--}1.7\text{ \AA}$  and (b)  $r = 1.9\text{--}2.9\text{ \AA}$  are shown.

or network, with bond angles  $\alpha = 120^\circ$  (as shown in Figure 6b, inset). This evidence clearly verifies that the cyanide anions reacted with each other and the reaction is partially irreversible.

Shifting of the peak position of the C–N pair clearly marks the process of the reaction. The maximum of the peak starts to move above 5 GPa and stops above 10 GPa, which correspond to the two transitions identified by *in situ* XRD. This is similar to the case of  $\text{K}_3\text{Fe}(\text{CN})_6$  under external pressure.<sup>5</sup> C–N peaks in the PDF patterns of  $\text{K}_3\text{Fe}(\text{CN})_6$  recovered from high pressure shift to greater radial distance when the applied pressure is above 8 GPa. This irreversible reaction between the cyano groups is attributed to the electron transfer to  $\text{Fe}^{3+}$ , which makes the product stable down to ambient pressure. Such an electron transfer may also happen in  $\text{Li}_3\text{Fe}(\text{CN})_6$  at 5 GPa, and the extent of reaction is much higher than that of  $\text{K}_3\text{Fe}(\text{CN})_6$ , as the conjugated C=N signal in the  $G(r)$  pattern is more intense than that of recovered  $\text{K}_3\text{Fe}(\text{CN})_6$ .

**Conductivity.** For a mixed electronic–ionic conductor, ionic and electronic conductivity can be distinguished by use of impedance spectroscopy. With blocking electrodes, the conducting ions cannot go through the electrode/sample interface. Hence the conductivity is mainly attributed to electronic conduction ( $1/R_e$ ) in the low-frequency limit and is attributed to the parallel connection of electronic conduction and ionic conduction ( $1/R_e + 1/R_i$ ) in the high-frequency limit. As shown in the Nyquist plot in Figure 7a, for high-frequency limit, an expression  $R_e R_i / (R_e + R_i)$  is approximately 0, suggesting that  $R_i \ll R_e$ . For this reason  $R_i$  cannot be determined accurately in the current plot, and here we mainly discuss the electronic transport. Within the van der Pauw configuration,<sup>12</sup> the resistivity and permittivity of the corresponding arc in the Nyquist plot was calculated. The permittivity of the semicircle was found to be around  $10^{-7}\text{ F}\cdot\text{cm}^{-1}$ , as calculated from the equation  $\omega_{\max} RC = \omega_{\max} \sigma \epsilon = 1$ .<sup>20</sup> The value is much larger than that typically reported for bulk material ( $10^{-12}\text{ F}\cdot\text{cm}^{-1}$ ) or even ferroelectric phases ( $10^{-9}\text{ F}\cdot\text{cm}^{-1}$ ). This large value of capacitance can be attributed to double layer capacitance. The capacitance per unit area of the electrode is approximately  $10^{-5}\text{ F}\cdot\text{cm}^{-2}$  (with the distance between electrodes around 0.01 cm), which is also within the range of double layer capacitance.<sup>21</sup> This indicates that while the electrons are conducting the ac current, the conducting ions are charging the interface double layer.

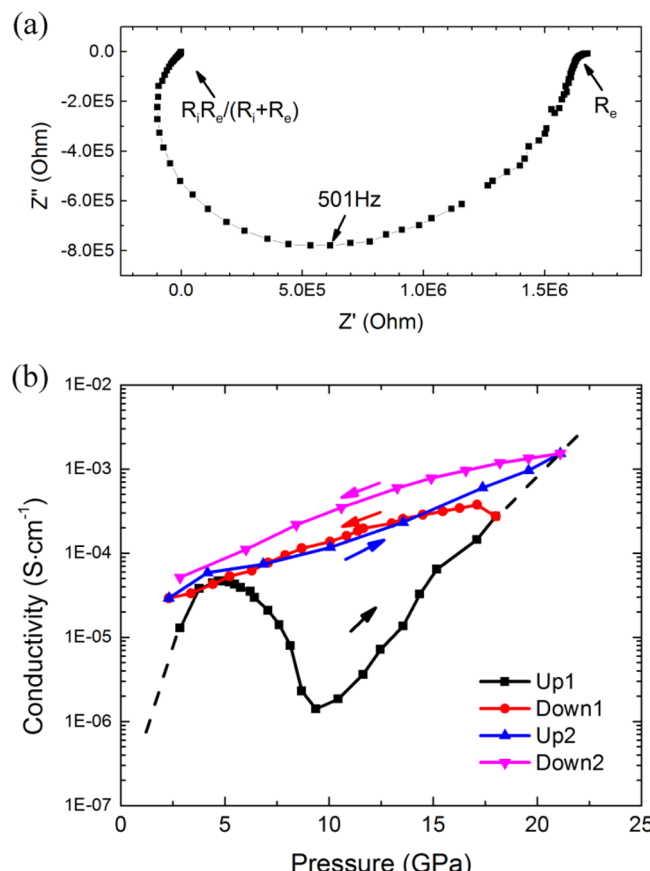


**Figure 7.** (a) Typical Nyquist plot of  $\text{Li}_3\text{Fe}(\text{CN})_6$  with van der Pauw configuration (at  $\sim 5\text{ GPa}$ ). (b) Electronic conductivity of  $\text{Li}_3\text{Fe}(\text{CN})_6$  under high pressure. The dashed line is by extrapolation.

As expected, the conductivity of  $\text{Li}_3\text{Fe}(\text{CN})_6$  was enhanced when external pressure was applied (Figure 7b). To keep a good sealing of the DAC, the conductivity at pressures lower than 2 GPa was not measured. From the extrapolation, the enhancement of conductivity is around 2 or 3 orders of magnitude. It was also reported that  $\text{Li}_3\text{Fe}(\text{CN})_6$  does not have a measurable conductivity ( $\sigma < 10^{-11}\text{ S}\cdot\text{cm}^{-1}$ ),<sup>22</sup> from which the enhancement is even greater. The enhancement is similar to that reported for  $\text{K}_3\text{Fe}(\text{CN})_6$ .<sup>1d</sup>

The conductivity reaches a local maximum at around 5 GPa, which is attributed to the beginning of II–III phase transition. This phase transition is similar to that in  $K_3Fe(CN)_6$  at 8 GPa. Both transitions feature decreasing conductivity and a shift of C–N peak in the  $G(r)$  patterns of recovered sample, with only minor changes in the XRD patterns. In  $K_3Fe(CN)_6$ ,  $Fe^{3+}$  is reduced to  $Fe^{2+}$  by  $CN^-$  ions, and  $CN^-$  ions bond to each other irreversibly.<sup>1d,5</sup> A similar reaction could also be an origin of the phase transition at 5 GPa in  $Li_3Fe(CN)_6$ . Above 10 GPa, when the II–III phase transition is finished, the conductivity increases again and keeps increasing above 20 GPa. The downloading curve is above the uploading curve, indicating some irreversible reaction continues as pressure increases. It is probably owing to another step of polymerization. This step is not found in the polymerization of  $K_3Fe(CN)_6$ , which clearly indicates the degree of polymerization of  $Li_3Fe(CN)_6$  is higher than that of  $K_3Fe(CN)_6$ .

## CONCLUSION

In conclusion, we designed and synthesized anhydrous  $Li_3Fe(CN)_6$ , determined its crystal structure, and investigated the PIP reaction and phase behavior under external pressure up to ~20 GPa. Three phase transitions have been found at around 1, 5, and 10 GPa by in situ XRD, Raman and impedance spectroscopy under high pressure, and neutron PDF investigations on the recovered sample. The cyanide groups in  $Fe(CN)_6^{3-}$  polymerize irreversibly above 5 GPa and undergo another step of reaction above 10 GPa. In comparison with the PIP of  $K_3Fe(CN)_6$ , the reaction pressure of  $Li_3Fe(CN)_6$  was successfully reduced down to industrially scalable levels, and the reaction extent of  $Li_3Fe(CN)_6$  is also much higher. This is mainly because  $Li^+$  is too small to be a barrier to the interaction between  $Fe(CN)_6^{3-}$ , and it reminds us the PIP reaction strongly depends on the crystal structure of the reactants. The conductivity of  $Li_3Fe(CN)_6$  is enhanced by more than 3 orders of magnitude as expected. With increasing pressure, the irreversible chemical reaction continues, leading to further increased conductivity.

## ASSOCIATED CONTENT

### Supporting Information

The Supporting Information is available free of charge on the ACS Publications website at DOI: [10.1021/acs.inorgchem.5b01851](https://doi.org/10.1021/acs.inorgchem.5b01851).

Two figures showing additional 1D XRD patterns collected at ambient and high pressure and Raman shift of C–N stretching mode of  $Li_3Fe(CN)_6$  under high pressure; two tables listing atomic coordinates, occupancies, and isotropic thermal displacement parameters for  $Li_3Fe(CN)_6$  at ambient and high pressure ([PDF](#))

## AUTHOR INFORMATION

### Corresponding Authors

\*(K.L.) E-mail [likuo@hpstar.ac.cn](mailto:likuo@hpstar.ac.cn).

\*(H.Z.) E-mail [zhenghy@hpstar.ac.cn](mailto:zhenghy@hpstar.ac.cn).

### Funding

This work was partially supported as part of the Energy Frontier Research in Extreme Environment (EFree) Center, an Energy Frontier Research Center funded by Basic Energy Sciences (BES), Department of Energy (DOE), under Award DE-SC0001057. W.Y. and H.-k.M. acknowledge financial support from DOE-BES X-ray Scattering Core Program

under Grant DE-FG02-99ER45775. We acknowledge the support of NSAF (Grant U1530402).

### Notes

The authors declare no competing financial interest.

## ACKNOWLEDGMENTS

We thank Dr. Chengdu Liang for discussion and Dr. Jong K. Keum for XRD measurement. In situ impedance spectroscopy was conducted at the Center for Nanophase Materials Sciences, which is a Department of Energy (DOE) Office of Science User Facility. A portion of this research was conducted at Spallation Neutron Source, which was sponsored by the Scientific User Facilities Division, Office of Basic Energy Sciences (BES), U.S. Department of Energy. SNAP is highly acknowledged for the sample synthesis. Neutron diffraction experiments at J-PARC were performed under Proposal 2014B0099.

## REFERENCES

- (a) Aoki, K.; Kakudate, Y.; Yoshida, M.; Usuba, S.; Tanaka, K.; Fujiwara, S. *Synth. Met.* **1989**, *28*, D91–D98. (b) Li, Y. L.; Luo, W.; Zeng, Z.; Lin, H. Q.; Mao, H. K.; Ahuja, R. *Proc. Natl. Acad. Sci. U. S. A.* **2013**, *110*, 9289–9294. (c) Aoki, K.; Baer, B. J.; Cynn, H. C.; Nicol, M. *Phys. Rev. B: Condens. Matter Mater. Phys.* **1990**, *42*, 4298–4303. (d) Li, K.; Zheng, H.; Ivanov, I. N.; Guthrie, M.; Xiao, Y.; Yang, W.; Tulk, C. A.; Zhao, Y.; Mao, H.-k. *J. Phys. Chem. C* **2013**, *117*, 24174–24180. (e) Khazaei, M.; Tripathi, M. N.; Kawazoe, Y. *Phys. Rev. B: Condens. Matter Mater. Phys.* **2011**, *83*, No. 134111. (f) Chall, M.; Winkler, B.; Milman, V. *J. Phys.: Condens. Matter* **1996**, *8*, 9049–9057. (g) Trout, C. C.; Badding, J. V. *J. Phys. Chem. A* **2000**, *104*, 8142–8145.
- (a) Nylen, J.; Konar, S.; Lazor, P.; Benson, D.; Haussermann, U. *J. Chem. Phys.* **2012**, *137*, No. 224507. (b) Chen, J. Y.; Yoo, C. S. *J. Chem. Phys.* **2009**, *131*, No. 144507. (c) Efthimiopoulos, I.; Kunc, K.; Vazhenin, G. V.; Stavrou, E.; Syassen, K.; Hanfland, M.; Liebig, S.; Ruschewitz, U. *Phys. Rev. B: Condens. Matter Mater. Phys.* **2012**, *85*, No. 054105.
- (a) Asakura, D.; Li, C. H.; Mizuno, Y.; Okubo, M.; Zhou, H.; Talham, D. R. *J. Am. Chem. Soc.* **2013**, *135*, 2793–2799. (b) Lu, Y. H.; Wang, L.; Cheng, J. G.; Goodenough, J. B. *Chem. Commun.* **2012**, *48*, 6544–6546.
- (a) Kulkarni, A.; Doll, K.; Schon, J. C.; Jansen, M. *J. Phys. Chem. B* **2010**, *114*, 15573–15581. (b) Heckathorn, J. W.; Kruger, M. B.; Gerlich, D.; Jeanloz, R. *Phys. Rev. B: Condens. Matter Mater. Phys.* **1999**, *60*, 979–983. (c) Chen, X. Q.; Fu, C. L.; Franchini, C. *J. Phys.: Condens. Matter* **2010**, *22*, No. 292201.
- (S) Li, K.; Zheng, H.; Wang, L.; Tulk, C. A.; Molaison, J. J.; Feygenson, M.; Yang, W.; Guthrie, M.; Mao, H. *J. Phys. Chem. C* **2015**, *119*, 22351–22356.
- Hattori, T.; Sano-Furukawa, A.; Arima, H.; Komatsu, K.; Yamada, A.; Inamura, Y.; Nakatani, T.; Seto, Y.; Nagai, T.; Utsumi, W.; Itaka, T.; Kagi, H.; Katayama, Y.; Inoue, T.; Otomo, T.; Suzuya, K.; Kamiyama, T.; Arai, M.; Yagi, T. *Nucl. Instrum. Methods Phys. Res., Sect. A* **2015**, *780*, 55–67.
- Sano-Furukawa, A.; Hattori, T.; Arima, H.; Yamada, A.; Tabata, S.; Kondo, M.; Nakamura, A.; Kagi, H.; Yagi, T. *Rev. Sci. Instrum.* **2014**, *85*, No. 113905.
- Mao, H.-k.; Bell, P. M. *Year Book - Carnegie Inst. Washington* **1976**, *75*, 824.
- Mao, H. K.; Xu, J.; Bell, P. M. *J. Geophys. Res.* **1986**, *91*, 4673–4676.
- Rivers, M.; Prakapenka, V. B.; Kubo, A.; Pullins, C.; Holl, C. M.; Jacobsen, S. D. *High Pressure Res.* **2008**, *28*, 273–292.
- Hammersley, A. P.; Svensson, S. O.; Hanfland, M.; Fitch, A. N.; Haussermann, D. *High Pressure Res.* **1996**, *14*, 235–248.
- van der Pauw, L. J. *Philips Res. Rep.* **1958**, *13*, 1–9.
- Klotz, S.; Hamel, G.; Frelat, J. *High Pressure Res.* **2004**, *24*, 219–223.

- (14) Neufeld, J.; Feygenson, M.; Carruth, J.; Hoffmann, R.; Chipley, K. K. *Nucl. Instrum. Methods Phys. Res., Sect. B* **2012**, *287*, 68–75.
- (15) Di Noto, V.; Vittadello, M.; Lavina, S.; Biscazzo, S.; Fauri, M. *Electrochim. Acta* **2003**, *48*, 2047–2058.
- (16) Wolski, W.; Milewski, J. *J. Therm. Anal.* **1979**, *15*, 79–92.
- (17) Bondi, A. *J. Phys. Chem.* **1964**, *68*, 441–451.
- (18) Figgis, B. N.; Skelton, B. W.; White, A. H. *Aust. J. Chem.* **1978**, *31*, 1195–1199.
- (19) Petricek, V.; Dusek, M.; Palatinus, L. Z. *Kristallogr. - Cryst. Mater.* **2014**, *229*, 345–352.
- (20) Irvine, J. T. S.; Sinclair, D. C.; West, A. R. *Adv. Mater.* **1990**, *2*, 132–138.
- (21) Boukamp, B. A. *Electrochemical Impedance Spectroscopy*; Presentation at University of Leiden, November 24–28, 2008; <http://www.lorentzcenter.nl/lc/web/2008/317/presentations/Boukamp.pdf>.
- (22) Tennakone, K.; Kaviratne, P. de S. *Phys. Status Solidi A* **1984**, *86*, K121–K123.